sustainability

MDPI

Article

Attribution Analysis of Long-Term Trends of Aridity Index in the Huai River Basin, Eastern China

Meng Li [1,†], Ronghao Chu [2,*,†], Abu Reza Md. Towfiqul Islam [3], Yuelin Jiang [1,*] and Shuanghe Shen [4]

1 School of Resources and Environment, Anhui Agricultural University, Hefei 230036, China; mengli@ahau.edu.cn
2 Anhui Public Meteorological Service Center, Anhui Meteorological Bureau, Hefei 230031, China
3 Department of Disaster Management, Begum Rokeya University, Rangpur 5400, Bangladesh; towfiq_dm@brur.ac.bd
4 Key Laboratory of Meteorological Disaster, Ministry of Education (KLME), Joint International Research Laboratory of Climate and Environment Change (ILCEC), Collaborative Innovation Center on Forecast and Evaluation of Meteorological Disasters (CIC-FEMD), Jiangsu Key Laboratory of Agricultural Meteorology, College of Applied Meteorology, Nanjing University of Information Science & Technology, Nanjing 210044, China; yqzhr@nuist.edu.cn
* Correspondence: ronghao_chu@163.com (R.C.); 1993047@ahau.edu.cn (Y.J.)
† These authors contributed equally to this work.

Received: 12 January 2020; Accepted: 24 February 2020; Published: 26 February 2020

Abstract: This paper aims to combinedly investigate the spatiotemporal trends of precipitation (Pre), reference evapotranspiration (ET_0), and aridity index (AI) by employing nonparametric methods based on daily datasets from 137 meteorological stations during 1961–2014 in the Huai River Basin (HRB). The dominant factors influencing ET_0 and AI trends were also explored using the detrended and differential equation methods. Results show that (1) Pre, ET_0, and AI were much larger in summer than in other seasons, and AI had a nonsignificant increasing trend in annual time scale, while Pre and ET_0 exhibited decreasing trends, but AI showed a downward trend in spring and autumn (becoming drier) and an upward trend during summer and winter due to increased Pre (becoming wetter); (2) lower AI values were identified in north and higher in south, and lower ET_0 was identified in south and higher in north in annual time scale, growing season and spring, while ET_0 decreased from west to east in summer and winter, the spatial distribution of Pre was similar to that of AI; (3) for ET_0 trends, in general, wind speed at two-meter height (u_2) was the dominant factor in spring, autumn, winter, and annual time scale, while in other seasons, solar radiation (R_s) played a dominant role; (4) for AI trends, AI was mostly contributed by Pre in spring, autumn, and winter, the R_s contributed the most to AI trend in growing season and summer, then in annual time scale, u_2 was the dominant factor; (5) overall, the contribution of Pre to AI trends was much larger than that of ET_0 in spring, autumn, and winter, while AI was mostly contributed by ET_0 in annual time scale, growing season and summer. The outcomes of the study may improve our scientific understanding of recent climate change effects on dry–wet variations in the HRB; moreover, this information may be utilized in other climatic regions for comparison analyses.

Keywords: precipitation; reference evapotranspiration; aridity index; detrending method; Huai River Basin

1. Introduction

Drought is one of the most serious manifestations of climate change and is of increasing concern for agriculture and human life in China, in which the dry land area is about 3.32×10^6 km^2 [1].

Wet and dry conditions are among the determining factors of the agroecosystem and other areas of concern such as ecology and human health. The Fourth and Fifth Assessment Reports of the Intergovernmental Panel on Climate Change (IPCC AR4 and AR5) pointed out that global climate will change at an unprecedented rate in the 21st century and the frequency of occurrence of extreme climatic events—such as intense rainfall; high temperatures; and heat waves, droughts, and floods—will also increase unprecedentedly [2,3].

In some current studies, the severity of climatic drought, namely aridity, in an area is usually measured by the drought index (aridity index, AI), which is the ratio of total annual precipitation to potential evapotranspiration [4]. The AI is a combination of precipitation and atmospheric evaporation demand (AED) and is determined by the effects of multiple climatic factors (precipitation, temperature, relative humidity, wind speed, solar radiation, etc.). Although precipitation and temperature are the two main indicators for evaluating climatic change, the AI can better express the significance of climate change in terms of the bioclimatic aspect [5]. Theoretically, in the context of global warming, the corresponding global terrestrial evaporation capacity should also increase due to rising temperatures [6]. However, an increasing number of studies have detected downward trends in reference evapotranspiration (ET_0) [7–12], potential evapotranspiration (ET_p) [13–16], and pan evaporation (E_{pan}) [6,17–22] in many parts of the world. The opposite change trend between temperature and evapotranspiration is the so-called evaporation paradox [23,24]. Many scholars have shown that evaporation trends are determined not by temperature alone, but also by the combined action of several climatic factors (such as solar radiation, relative humidity, wind speed, and so on) [12]. In addition, combined with precipitation, the aforementioned climatic factors can also determine the rates of evapotranspiration and runoff in a particular region. Although some studies have used extreme precipitation to show extreme drought or wetness events [25–28] and other aridity indices to evaluate the dry–wet condition of a region [29–31], only the effects of temperature and precipitation on dry and wet conditions were considered. At this point, the advantages of the AI for understanding the change characteristics of dry–wet conditions can be presented to the greatest extent. Furthermore, it also has scientific and practical applications for improving not only the comprehensive management of regional water resources in a basin but also the management of water-related natural disasters at the basin scale [32]. Since the AI is obtained by the precipitation divided by potential evapotranspiration, and potential evapotranspiration is mainly influenced by four main meteorological factors (temperature, relative humidity, wind speed, and solar radiation) [6,8,33,34]. Thus, clarifying the spatial and temporal trends of AI and determining the contributions of the above five meteorological factors to the AI trends are of greater importance for understanding regional scale dryness climate change features.

Some recent studies have reported drying or wetting trends in various parts of the world. For example, an increase in aridity has been observed in southwestern Spain [5], Iran [35,36], and southwest China [37], while a decrease in aridity has been detected in northwest China [10,38] and some areas of Iran [39]. However, the trends and causes of spatiotemporal AI variations in the Huai River Basin (HRB) of China have not been determined yet. According to the research evidence, it is estimated that 63 extreme floods and 46 extreme droughts occurred in the HRB during 1470–2010. Drought in the HRB led to famine throughout the basin and locust plague in most areas; furthermore, crops were severely destroyed, and some rivers were cut off. Some studies have also shown that the extreme climatic trends of droughts and floods in the HRB occur alternately at random [40]. As understanding climatic trends are vital to providing a scientific basis for regional water resource management and agricultural irrigation, especially in this warm temperate to subtropical region, it is necessary to study the changes and mechanisms of evapotranspiration and AI trends from a spatiotemporal perspective.

At present, the detrending [7,10,41] and differential equation [6,8] methods are widely applied for quantitative analysis of the influences of climatic factors on ET_0 and AI trends. The detrending method is simple and effective, mainly relying on a statistical and mathematical modeling approach, and provides the relative contributions of climatic factors on ET_0 and AI changes. As applied in previous studies, the

differential equation method is an approach to quantify the actual contribution of each meteorological factor to the trend in ET_0 based on the differential of the Penman–Monteith Food and Agriculture Organization (FAO) 56 model. However, the comparison between these two approaches has not been well documented in the existing literature. In addition, although the differential equation method has been applied to the study of the leading factors of AI trends, considering the daily precipitation is zero for much of the year, the contributions of other climatic factors to these trends might be ignored because the partial derivative of the climatic factor on the daily mean is multiplied by zero. As a result, the contributions of meteorological factors to the AI trends calculated by the differential equation method may produce great errors.

These problems regarding the studies of AI in the HRB have not been well documented in the literature. Thus, the objectives of this study are (1) to analyze the spatiotemporal variations of AI, precipitation (Pre), and ET_0 in the HRB; (2) to determine the dominant factors of ET_0 trends in annual and seasonal mean by the detrending method and discuss its applicability with the differential equation method as a reference; (3) to quantify the contributions of Pre and four main climatic factors to AI trends in annual and seasonal time scales in the whole HRB and its subregions; and (4) to determine the dominance of Pre and ET_0 in AI trends. It is anticipated that the outcomes of this research will give a basis for the comprehensive understanding of aridity regarding the recent impact of climate change and the effective management of regional water resources, thus to mitigate these adverse impacts of climate change on the water cycle and agricultural production and enhancing the regional ecological conservation.

2. Study Area and Data

The HRB, with a total catchment area of approximately 2.7×10^5 km^2, is located between the Yangtze River and Yellow River Basins in Eastern China (111°55′ E–121°25′ E and 30°55′ N–36°36′ N) (Figure 1). The HRB, belongs to temperate monsoon climate zoon, is also situated in a climate-transition zone from a warm temperate zone to a subtropical zone. The annual mean temperature varies from 13.2 °C to 15.7 °C, evaporation from 900 mm to 1500 mm, relative humidity between 66% and 81%, and wind speed between 1.3 $m{\cdot}s^{-1}$ and 3.5 $m{\cdot}s^{-1}$, while the annual precipitation is around 850 mm, with more than 50% occurring between June and September [42]. Due to the particular climate conditions and geographic location, the HRB plays a crucial role in China's agricultural sectors. During the half past century, waterlogged areas were widespread, accompanied by a prominent conflict between humans and water or land. Against the historical background, both the disordered Huai River water system and the deteriorated environment have aggravated the frequent occurrence of extreme events such as floods and droughts [33,42].

Daily climatic datasets from 137 meteorological stations in the HRB within the period 1961–2014 (Figure 1) were used in this study, provided by the National Meteorological Information Centre (NMIC) of the China Meteorological Administration (CMA). The datasets mainly include mean air temperature (T_a, °C), maximum air temperature (T_{max}, °C), and minimum air temperature (T_{min}, °C), relative humidity (RH, %), wind speed at 10 m height (u_{10}, $m{\cdot}s^{-1}$), sunshine duration (SD, h), precipitation (Pre, mm), and air pressure (P, kPa). Quality control of the meteorological datasets had already been carried out by staff at the NMIC. Moreover, we also defined five seasons according to the meteorological definition in the HRB, namely the growing season (April-October), spring (March-May), summer (June-August), autumn (September-November), and winter (December-February in next year).

In addition, to discuss the effects of atmospheric circulation, sea level pressure, air temperature in summer, air temperature in winter, geopotential height, and wind speed in summer at 500 hPa were derived from the ERA5 reanalysis data (https://www.ecmwf.int/en/forecasts/datasets/reanalysis-datasets/era5).

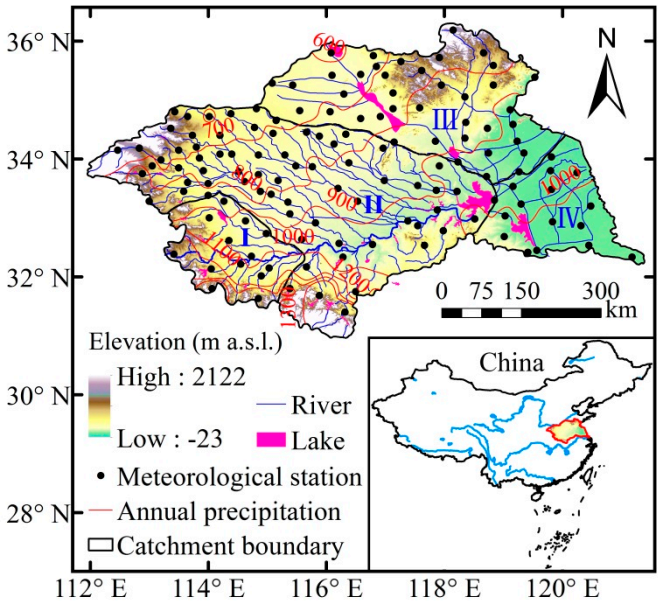

Figure 1. General situation and geographical location of Huai River Basin (HRB) in Eastern China. I, II, III, and IV are upper HRB, middle HRB, Yi-Shu-Si basin, and lower HRB, respectively. Digital elevation model (DEM) datasets of 90 m spatial resolution are available online (http://srtm.csi.cgiar.org/). The unit "m a.s.l." denotes the "meters above sea level".

3. Methods

3.1. Reference Evapotranspiration

In this study, the Penman–Monteith FAO 56 model was adopted to calculate the reference evapotranspiration (ET_0)

$$ET_0 = \frac{0.408\Delta(R_n - G) + \gamma\left(\frac{900}{T_a+273}\right)u_2(e_s - e_a)}{\Delta + \gamma(1 + 0.34u_2)} \quad (1)$$

where ET_0 is the reference evapotranspiration ($mm \cdot d^{-1}$); Δ is the slope of the vapor pressure curve ($kPa \cdot °C^{-1}$); R_n is the net solar radiation at crop surface ($MJ \cdot m^{-2} \cdot d^{-1}$); G is the soil heat flux density ($MJ \cdot m^{-2} \cdot d^{-1}$); γ refers to the psychrometric constant ($kPa \cdot °C^{-1}$); u_2 is the wind speed at 2 m height ($m \cdot s^{-1}$), which can be converted from wind speed at 10 m height by the formula calculation [43]; and e_s and e_a are saturation and actual vapor pressure, respectively (kPa). The detailed calculation formula can be found in the below and the literatures [8,41,43].

$$u_2 = u_z \frac{4.87}{\ln(67.8z - 5.42)}, \text{ where } z = 10 \quad (2)$$

$$e_a = e_s \times RH \quad (3)$$

$$e_s = 0.6108 \exp\left(\frac{17.27T_a}{T_a + 237.3}\right) \quad (4)$$

3.2. Aridity Index

The aridity index (AI) is calculated by the ratio of Pre to ET_0 (First calculate the daily ET_0 and Pre, and then add them to the annual or seasonal time scale to calculate the corresponding AI) as follows [36,44,45]:

$$AI = \frac{Pre}{ET_0} \quad (5)$$

where AI greater than 0.5 denotes humid conditions and lower than 0.5 indicates arid conditions. Smaller AI indicates drier conditions, and vice versa.

3.3. Trend Analysis

In this research, the Theil–Sen's slope estimator [46,47] was used to estimate the magnitude of the variables' trends. In addition, the nonparametric Mann–Kendall (M-K) test [48], which has been widely used in hydrological trend detection studies, was also applied to determine the significance of the variables' trends. Detailed descriptions of these methods can be found in Li et al. [6].

3.4. Detrending Method

To analyze the contributions of climatic factors to ET_0 and AI trends, the detrending method first proposed by Xu et al. [7] was employed in this study. The specific calculation steps are as follows [41]:

(1) Remove the change trends of Pre, ET_0, and climatic factors and convert them to fixed time series.

First, put the daily value data of a certain variable year by year into the column matrix one by one, generating a matrix with 366 rows and 54 columns, then establish a simple linear regression between the values of each row and the corresponding year (t) as follows:

$$z_t = bt + a \tag{6}$$

where z_t is the value of a fitted trend line, and a and b are fitting parameters.

Then remove the trend of variables by subtracting the z_t value from the original dataset. In order to avoid negative values of this subtraction operation, the first value z_1 is finally added, and the detailed formula is

$$y_t = x_t - z_t + z_1 \tag{7}$$

where x_t is the original time series of the certain variable, z_1 is the first value of z_t, and y_t is the final detrended data series. Finally, all detrended datasets are restored to the original data sequence. By the way, to maintain data consistency, only 365 days of data were selected here.

(2) Recalculate the certain variables using the detrended datasets.

After removing the change trends of certain variables, recalculate the daily ET_0 or AI during the past 54 years by using the detrended dataset of one variable and the original datasets of remaining variables.

(3) Compare the recalculated ET_0 or AI with the original one.

The difference between the recalculated ET_0 or AI and the original value is regarded as the contribution of that detrended variable to the ET_0 or AI trend. To better quantify this contribution, the evaluation index R is employed as follows:

$$R = \sum_{i=1}^{n} \frac{V^0(i) - V^R(i)}{V^0(i)} \tag{8}$$

where V^0 and V^R denote the original and recalculated annual (seasonal) ET_0 and AI, respectively, and n represents the length of the time series in years (here n = 54). The larger the absolute R value, the greater the contribution of the corresponding variable to the annual (seasonal) ET_0 or AI trend. $R > 0$, $R < 0$, and $R = 0$ denote positive, negative, and no contribution of the certain variable to ET_0 or AI trend, respectively.

3.5. Differential Equation Method

In order to compare with the detrending method, the differential equation method is also employed in this study. The principle of the differential equation method is to regard the ET_0 in Equation (1) as the combination of climatic factors. Thus, in our previous study, we improved the differential equation and selected four new climatic variables, namely mean temperature (T_a), relative humidity (RH), wind

speed at 2 m height (u_2), and solar radiation (R_s), as the main contributing factors [8]. The specific calculation formula is as below:

$$\frac{dET_0}{dt} = \frac{\partial ET_0}{\partial T_a}\frac{dT_a}{dt} + \frac{\partial ET_0}{\partial RH}\frac{dRH}{dt} + \frac{\partial ET_0}{\partial u_2}\frac{du_2}{dt} + \frac{\partial ET_0}{\partial R_s}\frac{dR_s}{dt} + \varepsilon \quad (9)$$

Each term on the right side of the formula represents the contribution of T_a, RH, u_2 and R_s to ET_0, respectively. ε represents the error term between the calculated ET_0 trends and the ET_0 trends estimated by Theil-Sen's estimator.

The detailed calculation of R_n in Equation (1) and R_s in Equation (9) are shown as follows:

$$R_s = \left(a_s + b_s\frac{SD}{N}\right)R_a \quad (10)$$

$$R_n = R_{ns} - R_{nl} \quad (11)$$

$$R_{ns} = (1-\alpha)R_s \quad (12)$$

$$R_{nl} = \sigma\left(\frac{T_{max,K}^4 + T_{min,K}^4}{2}\right)\left(0.34 - 0.14\sqrt{e_a}\right)\left(1.35\frac{R_s}{R_{s0}} - 0.35\right) \quad (13)$$

where a_s and b_s are regression coefficients, N refers to maximum possible sunshine hours (h), R_a refers to extraterrestrial radiation ($MJ{\cdot}m^{-2}{\cdot}day^{-1}$), R_{ns} refers to incoming net shortwave radiation ($MJ{\cdot}m^{-2}{\cdot}day^{-1}$), R_{nl} refers to net outgoing longwave radiation ($MJ{\cdot}m^{-2}{\cdot}day^{-1}$), α refers to the albedo of reference crop (value of 0.23), $T_{max,K}$ and $T_{min,K}$ refer to the maximum and minimum absolute temperature during 24 h (K = °C + 273.16), R_{s0} refers to clear-sky radiation. More detailed calculation process can be referred to Allen et al. [43] and Li et al. [8].

4. Results

4.1. Temporal Variations of AI, ET_0, and Pre

Figure 2 presents the monthly variation characteristics of Pre, ET_0, and AI in the HRB. All three were much larger in summer than in other seasons. In April and May, the minimum value of AI was about 0.6 because the difference between ET_0 and Pre reached the peak. In July, the difference between Pre and ET_0 also reached the peak, which generated the sharp increase and maximum AI.

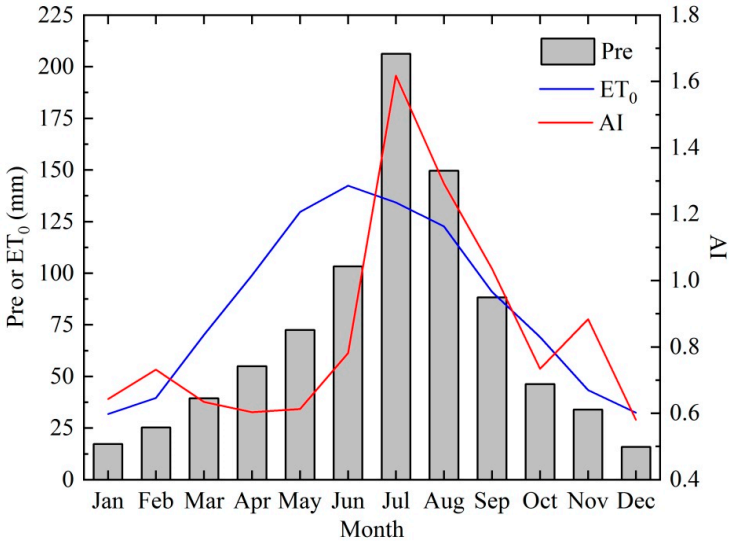

Figure 2. Monthly variation characteristics of aridity index (AI), reference evapotranspiration (ET_0), and precipitation (Pre).

Table 1 lists annual, growing season, and seasonal trends of AI, Pre, and ET_0 in each subregion of the HRB. At annual time scale, AI increased throughout the region, while Pre and ET_0 decreased. The specific change trends of AI, Pre, and ET_0 can be seen in Supplementary Figure S1. Similar results can also be detected in the growing season. Generally speaking, the changing trends of AI and Pre were not significant in each region and time scale. ET_0 exhibited much more significance than Pre. Moreover, AI and Pre show consistent increasing trends in summer and winter and decreasing trends in spring and autumn in the whole region and in all subregions. To facilitate the reader's understanding and save space, the temporal trends of other climate factors can be found in Supplementary Table S1.

Table 1. Temporal trends of AI, Pre, and ET_0 in each subregion and each time scale of the HRB.

Region	Variable	Annual		Growing Season		Spring		Summer		Autumn		Winter	
		Z	β	Z	β	Z	β	Z	β	Z	β	Z	β
Upper	AI	0.13	0.0003	0.12	0.0004	−0.84	−0.0031	1.30	0.0063	−1.31	−0.0058	0.58	0.0025
	Pre	−0.58	−1.269	−0.48	−1.158	−0.78	−0.753	0.58	0.725	−1.85	−1.257	0.55	0.170
	ET_0	−3.49	−1.787 ***	−3.55	−1.578 ***	0.69	0.197	−4.97	−1.567 ***	−1.76	−0.253	−1.12	−0.138
Middle	AI	1.19	0.0019	1.19	0.0016	−0.15	−0.0005	1.81	0.0055	−0.67	−0.0024	0.88	0.0025
	Pre	−0.28	−0.365	−0.42	−0.470	−0.42	−0.207	0.45	0.407	−0.95	−0.711	0.75	0.158
	ET_0	−4.74	−2.561 ***	−4.92	−2.287 ***	−1.06	−0.331	−5.43	−1.596***	−2.73	−0.400 **	−1.82	−0.235
Yi-Shu-Si	AI	−0.09	−0.0002	−0.22	−0.0006	−0.01	−0.0001	0.57	0.0018	−0.12	−0.0008	0.24	0.0005
	Pre	−0.98	−1.498	−1.15	−1.618	0.00	−0.015	−0.37	−0.426	−0.49	−0.328	0.27	0.049
	ET_0	−3.88	−1.556 ***	−3.83	−1.446 ***	−0.60	−0.153	−4.43	−1.094 ***	−2.25	−0.276 *	−0.39	−0.044
Lower	AI	−0.28	−0.0008	−0.93	−0.0025	−1.30	−0.0042	0.81	0.0049	−1.15	−0.0039	1.00	0.0048
	Pre	−0.16	−0.328	−0.85	−1.787	−0.75	−0.461	0.70	0.929	−1.37	−0.795	1.49	0.562
	ET_0	0.45	0.177	0.15	0.062	3.04	0.660 **	−1.97	−0.498 *	0.91	0.100	0.93	0.075
Whole	AI	0.57	0.0009	0.22	0.0004	−0.51	−0.0010	1.31	0.0042	−0.61	−0.0022	0.82	0.0022
	Pre	−0.75	−0.942	−1.06	−1.343	−0.33	−0.182	0.21	0.299	−1.04	−0.654	0.75	0.194
	ET_0	−4.09	−1.894 ***	−4.25	−1.772 ***	−0.39	−0.122	−4.64	−1.307 ***	−2.40	−0.308 *	−1.24	−0.143

Note: *, **, and *** denote significance levels of 0.05, 0.01, and 0.001, respectively. β is the estimated slope trend of AI, Pre, and ET_0. $\beta > 0$ and $\beta < 0$ signify upward and downward trend, respectively. Z is the Mann–Kendall test statistic.

4.2. Spatial Variations of AI, ET_0, and Pre

The spatial distribution of the AI is shown in Figure 3. Overall, lower AI values were identified in the north and higher in the south. The AI at 69.3% of stations exhibited an upward trend in the HRB at an annual time scale. Moreover, significant increasing AI trends were identified in the northern part of the middle HRB. Similar spatial patterns can also be found during the growing season. In summer, AI was higher than in other seasons and about 89.7% of stations exhibited an upward trend. During winter, the spatial distribution of AI value was similar to that in spring, with 89.1% of stations showed an increasing trend.

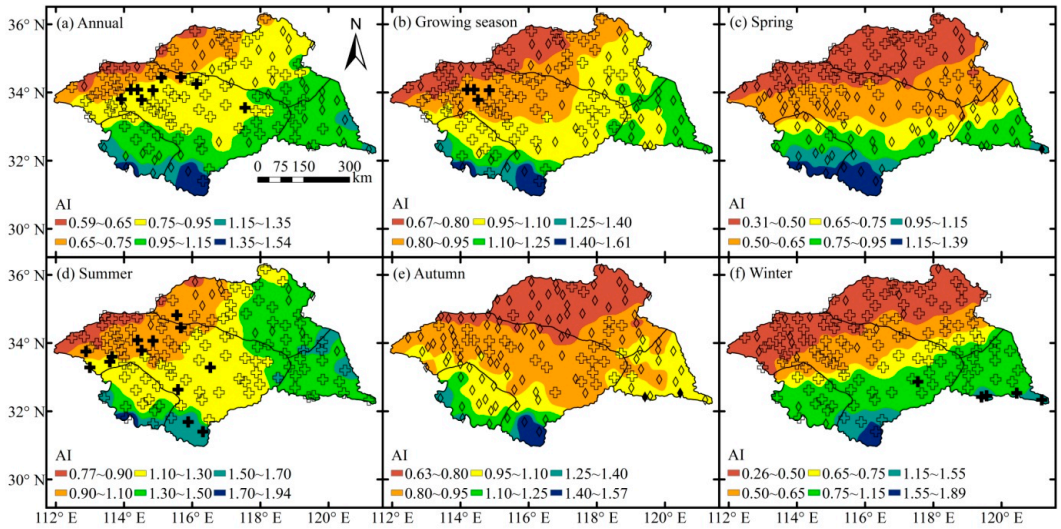

Figure 3. Spatial variation of AI during each time period in the HRB. Note: Solid and hollow plus signs represent significant and nonsignificant increasing trends, respectively; solid and hollow rhombuses represent significant and nonsignificant decreasing trends, respectively. Significance level is 0.05.

Spatial variation characteristics of ET_0 in different time scales are shown in Figure 4. Overall, lower ET_0 was identified in the south and higher in the north annually and in growing season and spring, while ET_0 decreased from west to east in summer and winter. In the annual time scale, low ET_0 values were found in the southern upper and middle HRB and high values in the northern middle HRB and Yi-Shu-Si basin. Similar spatial patterns could be found in the growing season. In spring, stations showing a significant downward trend were mainly distributed in the northern part of the middle HRB and Yi-Shu-Si basin, and a significant upward trend in the southwest upper and middle and most of the lower HRB. During summer, ET_0 was higher than in other seasons, and almost all the stations exhibited a significant downward trend. During autumn, ET_0 also exhibited an overall downward trend. The stations with significant trends were less than those in summer. Moreover, stations with significantly decreasing and increasing ET_0 were concentrated in the northern and lower HRB, respectively. During winter, ET_0 was the lowest of the four seasons. Stations with significantly decreasing ET_0 were mainly located in the northwest of middle HRB.

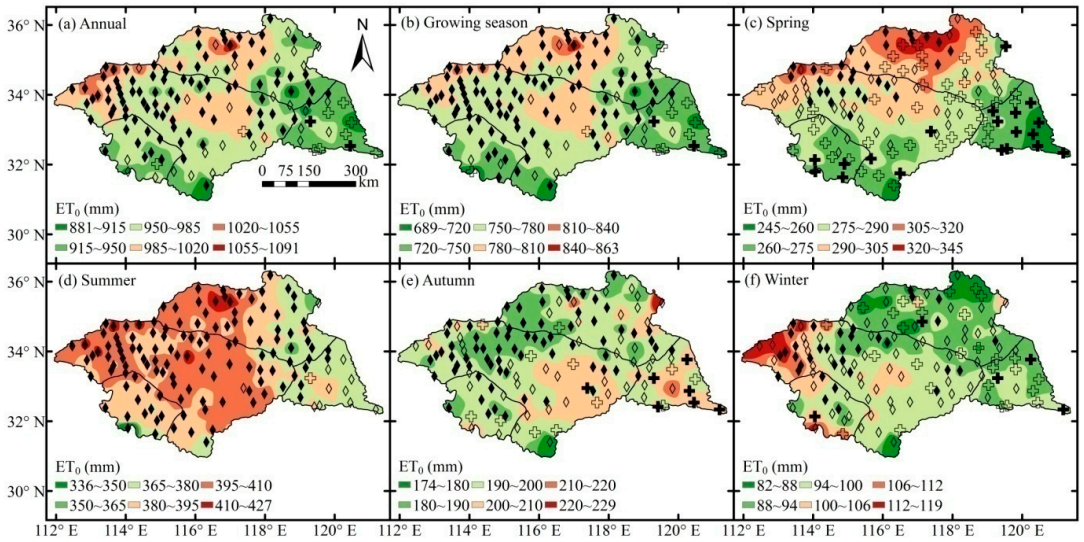

Figure 4. Spatial variation of ET_0 during each time period in the HRB. Note: Solid and hollow plus signs represent significant and nonsignificant increasing trend, respectively; solid and hollow rhombuses represent significant and nonsignificant decreasing trend, respectively. Significance level is 0.05.

The spatial distribution of Pre is shown in Figure 5. Similar to the distribution of AI, lower Pre values were also found in the north and higher in the south. A similar spatial pattern of Pre trends can be detected during the growing season. In summer, Pre was evidently higher than in other seasons. In autumn, the number of stations with a decreasing Pre trend increased significantly, accounting for approximately 89.8% of all stations. During winter, the Pre value was the smallest in the four seasons. The spatial pattern of Pre was similar to that in spring. However, about 83.2% of stations showed an increasing trend, and those with a significantly increasing trend were mainly identified in the southeastern middle and lower HRB.

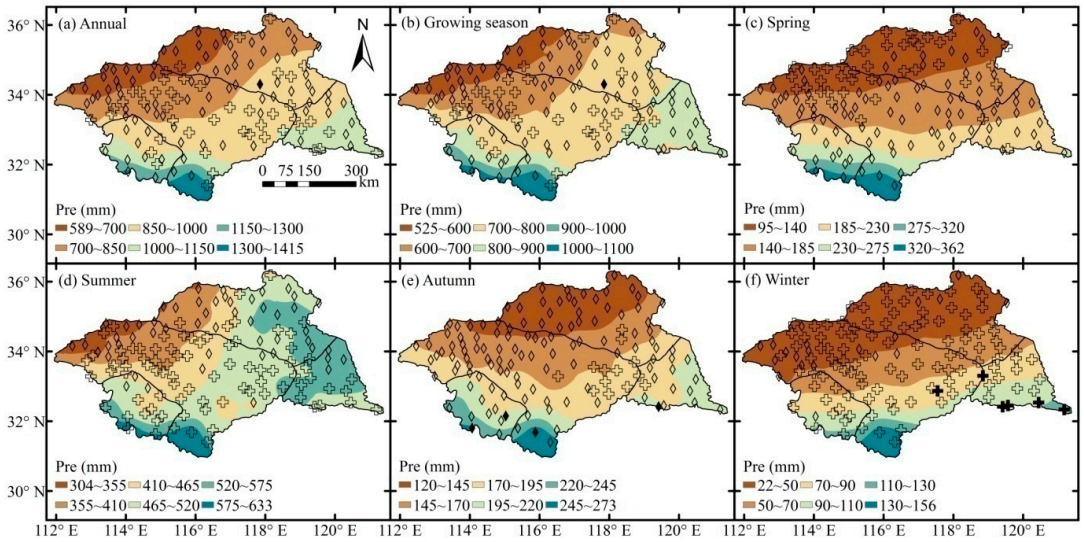

Figure 5. Spatial variation of Pre during each time period in the HRB. Note: Solid and hollow plus signs represent significant and nonsignificant increasing trend, respectively; solid and hollow rhombuses represent significant and nonsignificant decreasing trend, respectively. Significance level is 0.05.

4.3. Original and Detrended Trends of AI, ET_0, Pre, and Other Climatic Factors

The original and detrended AI, ET_0, Pre, and climatic parameters for annual time scale in the HRB during 1961–2014 are shown in Figure 6. The original ET_0 indicated a significant decreasing trend,

thus the detrended ET_0 was larger than the original one (Figure 6b). The detrended AI and Pre were not distinguished from the original, as they did not change obviously during 1961–2014 (Figure 6a,c). With the proportional relationship between AI and Pre, the significant decreasing ET_0 trend cannot be recognized in the AI trend. This phenomenon was caused by the decreasing ET_0 trend was too small to change the AI trend in their inverse proportional relationship (Table 1). The original T_a showed an upward changing trend, which resulted lower detrended data (Figure 6d). Moreover, the original RH, u_2, and R_s showed a downward changing trend, which caused larger detrended data (Figure 6e–g). The biggest difference between the original and detrended data was observed in u_2 (Figure 6f).

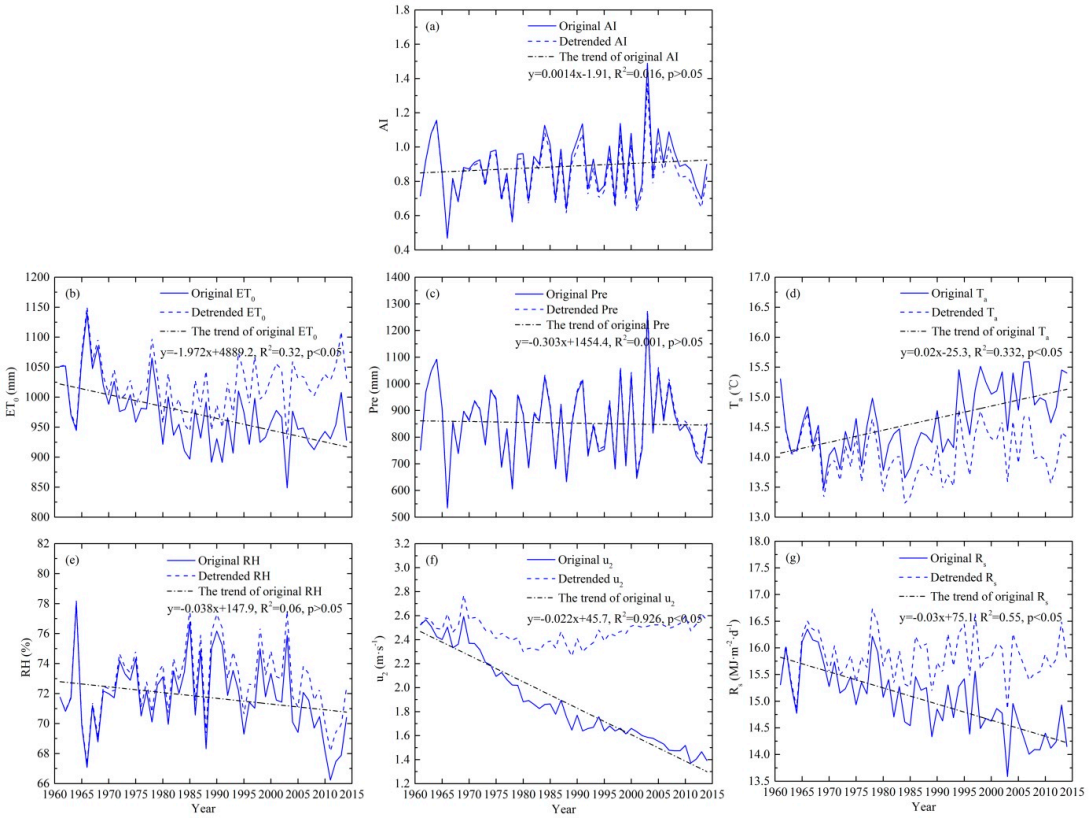

Figure 6. Original and detrended AI, ET_0, Pre, and other climatic parameters in the HRB during 1961–2014: (**a**) AI; (**b**) ET_0; (**c**) Pre; (**d**) mean air temperature (T_a); (**e**) relative humidity (RH); (**f**) wind speed at 2 m height (u_2); (**g**) solar radiation (R_s).

For the present study, the main reason for the declining u_2 can be explained by the following: (1) large-scale atmospheric circulation patterns caused by climate warming [49], (2) reduced temperature and pressure gradients [50], (3) gradually weakening Siberian high and East Asian monsoon systems [7], (4) enhancement of the Asian zonal circulation pattern [51], and (5) acceleration of urbanization and associated changes in aerosol/dust concentrations caused by the specific characteristics and socioeconomic conditions of different geographical locations [52–54]. In addition, the reasons for the decreasing R_s trend during the past 54 years mainly include (1) aggravating air pollution and increasing aerosol loading due to anthropogenic effluent pollutants [55], (2) increasing energy consumption and regional cloud cover [56–58], and (3) the significant decreasing u_2 also inhibited the diffusion of pollutants and aerosols [59]. Although we have listed the possible reasons for the decrease in u_2 and R_s, the main reasons for the decrease in u_2 and R_s in the HRB are still uncertain and need to be further investigated.

4.4. Contributions of Four Main Climatic Factors to ET_0 Trends

The R_{ET0} index was calculated to evaluate the effects of four main climatic factors on ET_0 trends in this study. In order to verify the effectiveness of the detrending method, the differential equation method was also adopted here (Figure 7). Specific values of R_{ET0} and the contributions calculated by the differential equation method (C_{ET0}) in each subregion and time scale can also be found in Supplementary Table S2. From Figure 7 and Table S2, we found the dominant factors and the order of influence factors of ET_0 trends calculated by these two methods are highly consistent. Thus, we believe the results calculated by the detrending method in this study is reasonable and reliable.

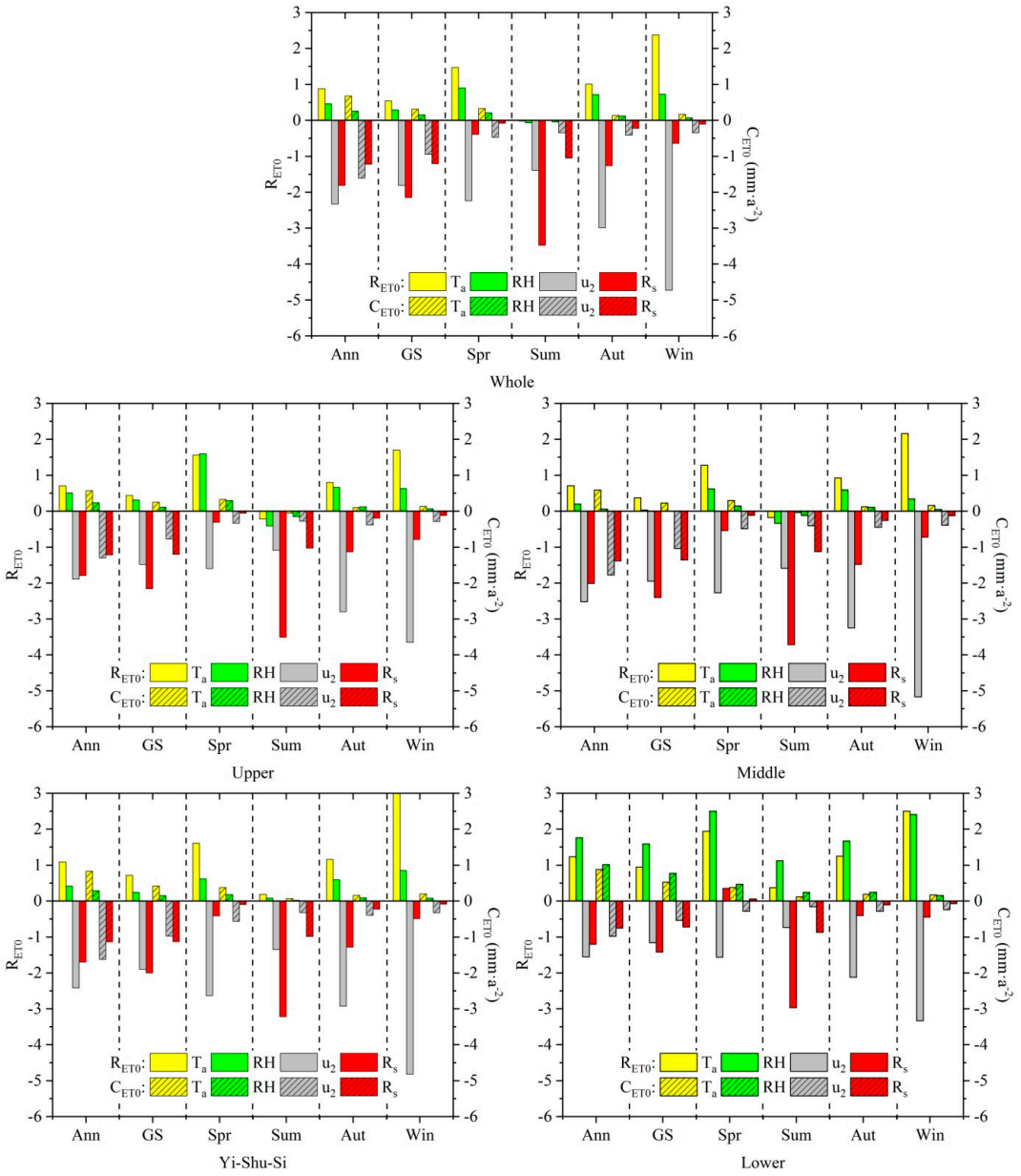

Figure 7. Contributions of climatic factors to ET_0 trends in each time scale and subregion of the HRB when using the detrending method (R_{ET0}, where R_{ET0} is dimensionless) and the differential equation method (C_{ET0}, mm·a^{-2}). Note: The bar graph with pure color and shadow indicated the R_{ET0} and C_{ET0} respectively. Ann, GS, Spr, Sum, Aut, and Win are the abbreviations for annual, growing season, spring, summer, autumn, and winter, respectively.

For the whole HRB, u_2 was the dominant factor of ET_0 trends in spring, autumn, winter, and annual time scale, while in other seasons (growing season and summer), R_s played a dominant role. Similar findings can also be found in the upper middle HRB and Yi-Shu-Si basin. In the lower HRB in spring, growing season, and annual time scale, the dominating factor of ET_0 trends shifted to RH. In addition, RH shared the dominant position with u_2 in the upper HRB in spring.

Furthermore, T_a and RH made positive contributions to ET_0 trends in all time scales except for summer in the whole HRB and all subregions. In summer, positive contributions of T_a and RH were only found in Yi-Shu-Si basin and lower HRB. Moreover, u_2 and R_s made negative contributions in each time scale and each region, but positive contributions in the lower HRB in spring. Generally speaking, for most regions (upper, middle, and the whole HRB as well as the Yi-Shu-Si basin) in all time scales, the positive contributions of T_a and RH were not able to offset the negative ones of u_2 and R_s, which ultimately led to the overall downward trend in ET_0. Nevertheless, in the upper HRB in spring, the increased contributions of T_a and RH and the decreased contribution of R_s eventually led to an upward ET_0 trend. A similar phenomenon could also be found in the lower HRB except in the summer season. All the results in Figure 7 can provide reasonable explanations for the ET_0 trends in Table 1. In addition, right behind u_2, T_a was the second dominant factor affecting ET_0 trends, especially in spring and winter.

For better understanding, the contribution characteristics of four main climatic factors to ET_0 trends, the spatial distribution characteristics of dominant factors influencing ET_0 variation trends are shown in Figure 8. In the annual time scale, ET_0 variation trends at most stations were dominated by u_2. The ET_0 trends in the upper and middle HRB and Yi-Shu-Si basin were mainly dominated by u_2 and R_s, and by RH in the lower HRB. In the growing season, R_s dominated the ET_0 trends in most of the HRB and the spatial distribution of dominant factors was similar to that in the annual time scale. In spring, u_2 dominated the ET_0 variation trends at most stations, and RH also played a dominant role in ET_0 trends in some stations of lower HRB and southern parts of the upper and middle HRB, while the rest of the subregions were mainly dominated by T_a. In summer, R_s played an absolute leading role in almost the whole region. In autumn, u_2 also dominated the ET_0 trends at most stations, and RH also played dominant roles in some stations of lower HRB. In winter, the spatial distribution of dominant factors was similar to that in autumn.

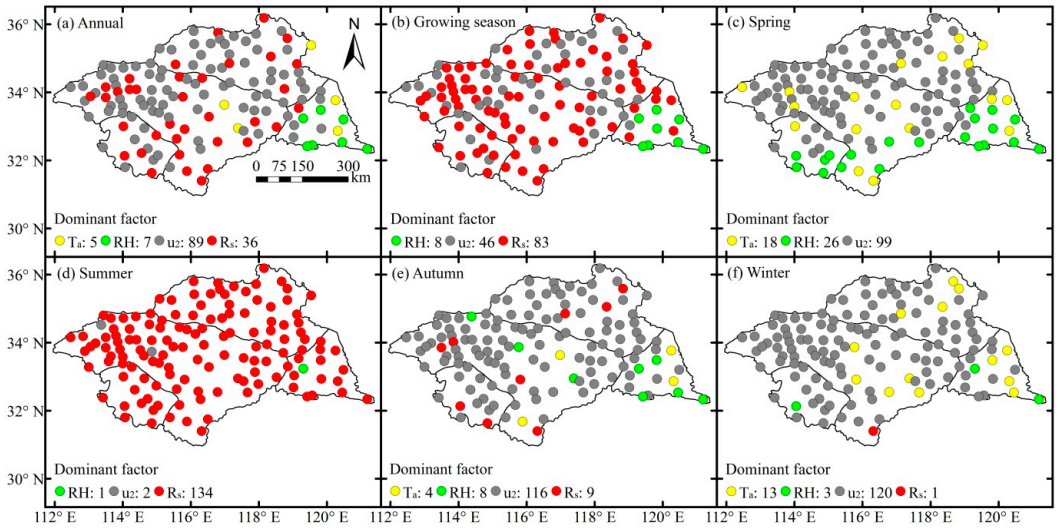

Figure 8. Spatial distribution characteristics of dominant factors influencing ET_0 variation trends. Note: Numbers represent stations dominated by corresponding climatic factors.

4.5. Contributions of Pre and Four Main Climatic Factors to AI Trends

To evaluate the effects of Pre and four main climatic factors on AI, the R_{AI} index was employed in this research (Figure 9). Specific values of the R_{AI} index for each time scale in the whole HRB and each subregion in different time scales can be found in Supplementary Table S3.

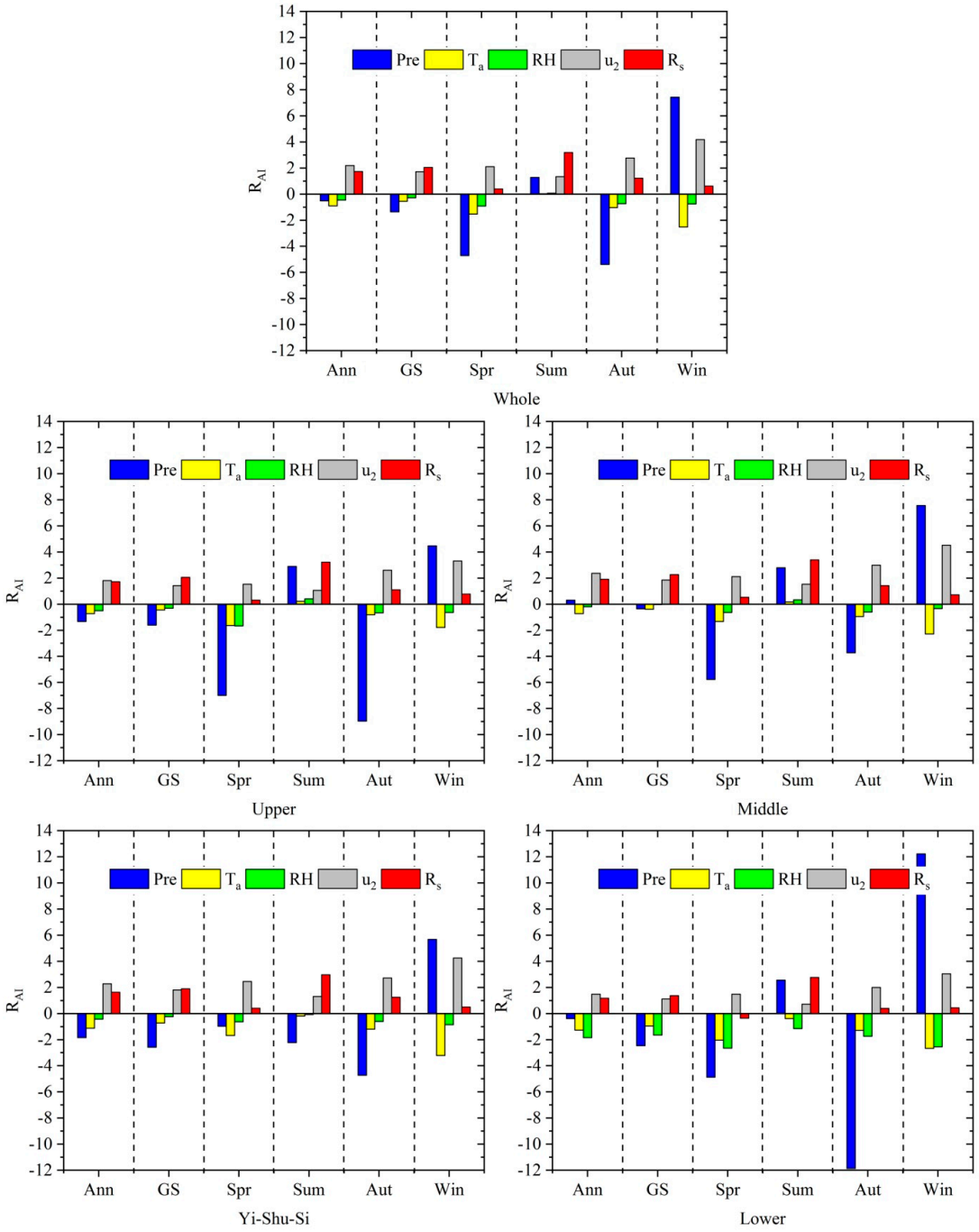

Figure 9. Contributions of Pre and four main climatic factors to AI trends in each time scale and subregion of the HRB. Note: Ann, GS, Spr, Sum, Aut, and Win are the abbreviations for the annual, growing season, spring, summer, autumn, and winter, respectively.

Generally, AI was mostly contributed by Pre in spring, autumn, and winter. The R_s contributed the most to AI trend in growing season and summer. Then in annual time scale, u_2 was the dominant factor. However, in the Yi-Shu-Si basin, the dominant factor of AI trends in the growing season shifted to Pre. Moreover, in the lower HRB, the dominant factor of AI trends in annual time scale was RH and then shifted to Pre in the growing season and spring.

Mostly, the positive/negative contribution of the dominant factor led to the increase/decrease trend of AI combined with the AI trends shown in Table 1. Specifically, Pre generally made a negative contribution to AI trends in the growing season, spring, autumn, and annual time scale, and a positive contribution in summer and winter. The contributions of T_a and RH were negative and those of u_2 and R_s were positive in general. However, in summer, Pre and other climatic factors contributed positively to AI trends in the upper, middle, and whole HRB. In the growing season and annual time scale, the positive contributions of u_2 and R_s offset the negative ones of Pre, T_a, and RH, which ultimately led to positive AI trends in the upper, middle, and whole HRB. Nevertheless, the negative contributions of Pre, T_a, and RH were greater than the positive ones of u_2 and R_s, which eventually led to negative AI trends in the Yi-Shu-Si basin and lower HRB during the same period. The AI trends in spring and autumn can be interpreted similarly. Different from other seasons, although Pre, T_a, and RH had negative contributions in the Yi-Shu-Si basin, they could not offset the positive contributions from u_2 and R_s. Similarly, negative contributions from T_a and RH in the lower HRB could not offset the positive contributions from Pre, u_2, and R_s. These eventually led to the increasing AI trend during the summer. Similarly, the upward trend of AI in winter can also be well explained. Due to the smaller AI trend in the Yi-Shu-Si basin during spring and annual time scale, the results in Figure 9 differ from those in Table 1.

The spatial distribution characteristics of dominant factors influencing AI trends are shown in Figure 10. In the annual time scale, the dominant factors in AI variation trends were u_2, followed by Pre, R_s, RH, and T_a, while the AI trends in the lower HRB were mainly dominated by RH and Pre. In the growing season, Pre dominated the AI trends in most areas of the HRB and the proportion of R_s dominated stations increased, accounting for about 32.1%. This phenomenon was inconsistent with the result in Figure 9, which indicated that the R_s was the dominant factor in the whole HRB in the corresponding period. The specific reasons for this phenomenon are the positive and negative contributions of Pre to the AI trends offset each other in stations. Meanwhile, the contributions of R_s and u_2 are basically positive, which ultimately led to the smaller contribution of Pre and larger contribution of R_s and u_2 on the average in the whole region. In addition, the spatial distribution of dominant factors was similar to that in the annual time scale. In spring, Pre still dominated the AI variation trends in 77.4% of stations, while u_2 dominated stations mainly distributed in the Yi-Shu-Si basin. In summer, R_s and Pre were both dominant factors in almost the whole region. In autumn, Pre also dominated the AI variation trends in most stations, while u_2 and Pre were the dominant factors in the Yi-Shu-Si basin and northeast middle HRB. In winter, T_a and u_2 dominated the AI trends in the northern Yi-Shu-Si basin, and u_2 and Pre were the dominant factors in the western middle HRB, and other subregions were mainly dominated by Pre.

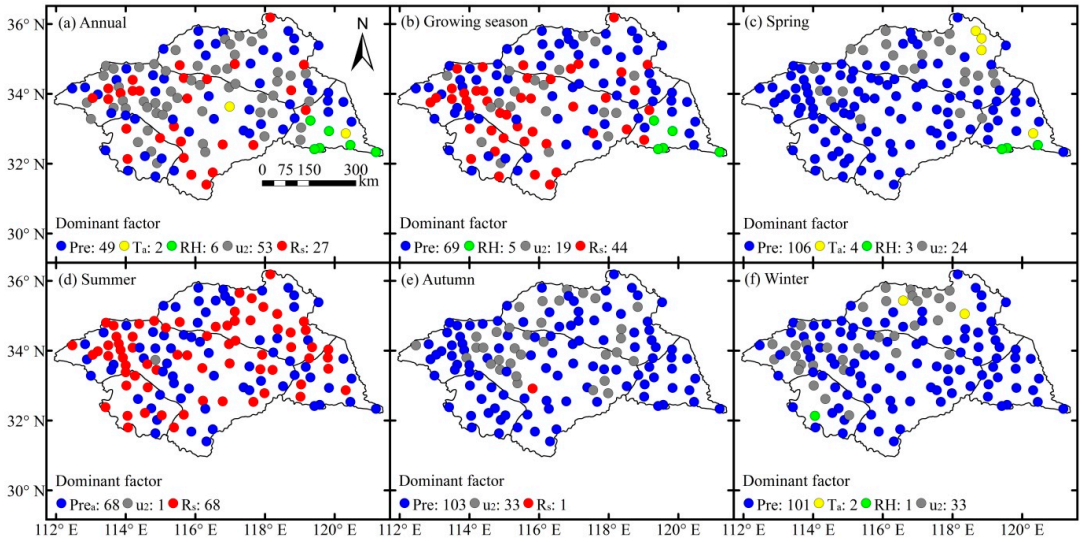

Figure 10. Spatial distribution characteristics of dominant factors influencing AI variation trends. Note: Numbers represent stations dominated by corresponding climatic factors.

4.6. Contributions of Pre and ET_0 to AI Trends

The contributions of Pre and ET_0 to AI trends in each time scale and subregion during 1961–2014 are shown in Figure 11. Specific values can be found in Supplementary Table S4. Overall, echoed with the result in Section 3.5, the contribution of Pre was much larger than ET_0 in spring, summer and winter, in which only showed positive contribution in winter. Moreover, AI was mostly contributed by ET_0 in summer. Thus, AI was dominated by ET_0 in annual time scale and growing season, which was the result of the positive and negative contributions of Pre in different seasons offset each other. As shown, for the whole HRB, ET_0 contributed positively to the AI trend in all time scales except for spring, and Pre made a positive contribution to the AI trend in summer and winter and a negative contribution in other time scales. Moreover, AI was affected more by ET_0 in the growing season, summer, and annual time scale, and by Pre in other seasons. Similar findings can also be detected in the upper and middle HRB and Yi-Shu-Si basin. However, in the lower HRB, Pre played a dominant role in the AI trend except for annual time scale. As shown in Table 1, in the upper, middle, and whole HRB and the Yi-Shu-Si basin, ET_0 exhibited a significant decreasing trend, especially in the growing season, summer, and annual time scale, when the dominant factor of AI trend was ET_0. Here, the significance of ET_0 was significantly related to its dominance in AI trends. However, in the lower HRB, ET_0 exhibited a significant decreasing trend only in spring and summer, its significance was evidently weaker than in other subregions, and the dominant factor was Pre. Considering the particularity of the lower HRB, the relationship between the significance of Pre and ET_0 and their dominance in AI trends is not obvious. Similar specificity of the lower HRB can also be found in our previous studies [6,8]. The specific reasons for this phenomenon remain to be further investigated.

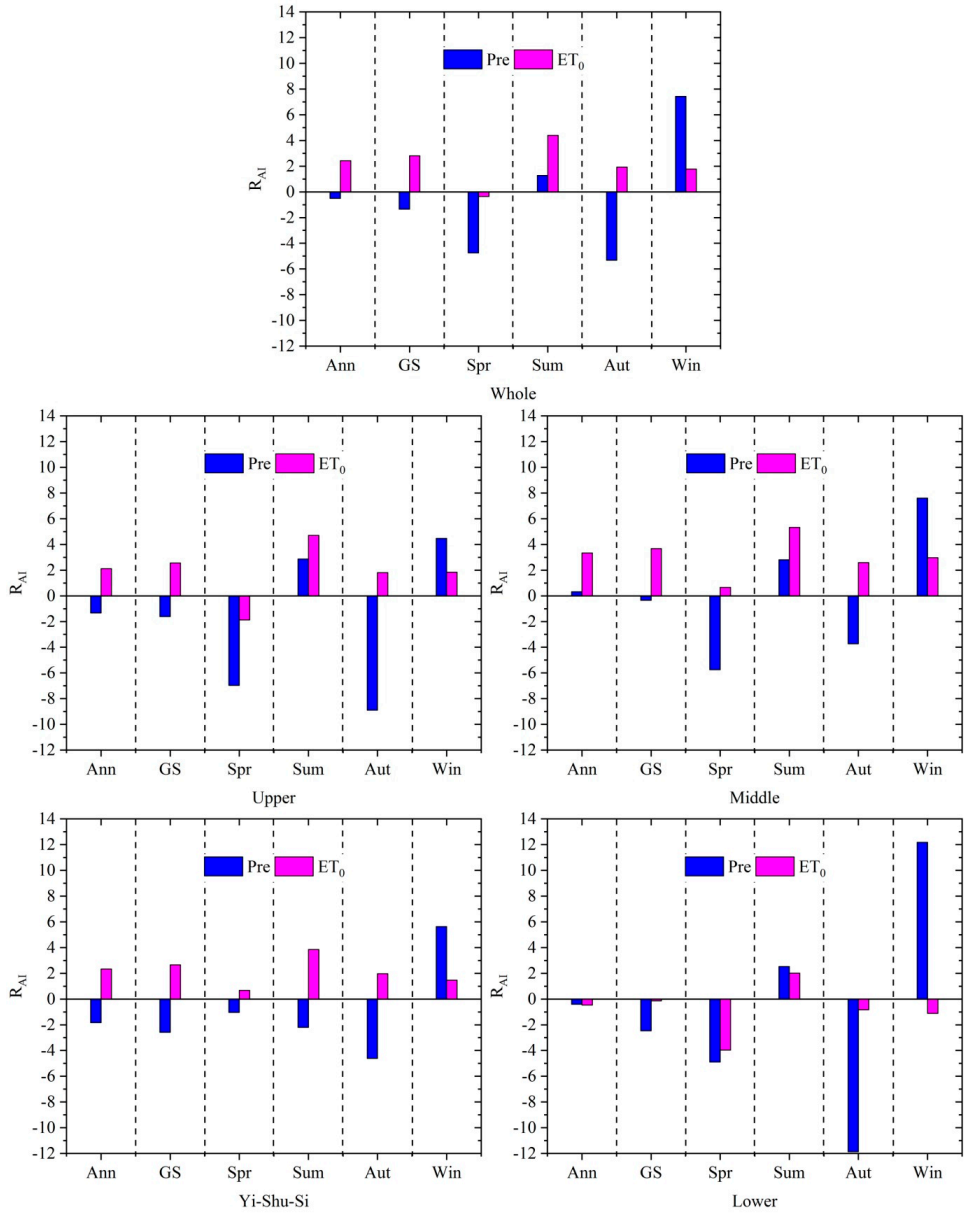

Figure 11. Contributions of Pre and ET_0 to AI trends in each time scale and subregion of the HRB. Note: Ann, GS, Spr, Sum, Aut, and Win are the abbreviations for the annual, growing season, spring, summer, autumn, and winter, respectively.

5. Discussion

In this study, we compared the differential method with the detrending method to determine the leading factors of ET_0 trends, and found that the results with the detrending method were pretty much the same as those in our previous research of the HRB with the differential equation method (Supplementary Table S2) [8]. This further proves the effectiveness and reliability of the detrending method when quantitatively analyzing the causes of ET_0 and AI trends in the HRB and other regions.

In previous studies, many scholars explored AI trends in China. Huo et al. [10] investigated the effects of climate change on AI in arid northwest China and stated that increasing Pre was the most sensitive climatic factor and made a much greater contribution than decreasing ET_0 to the downward AI trend (calculated by $(ET_0–Pre)/ET_0$). A similar area of northwest China showed similar findings [38]. In addition, the AI calculated with the same formula in the Loess Plateau [60], Tibetan Plateau [61], Yellow River Basin [32], and southwest China [62] and with the ratio between ET_0 and Pre in Northwest

China [38] showed a declining trend, which indicated that these regions became wetter in the past 50 years. Considering the correlation coefficient between AI and climate factors, the dominant factor of the AI trend in the Yellow River basin was determined to be RH, followed by Pre [32]. In order to understand the variation of AI more concretely in northern China, Zhang et al. [63] used 283 standard meteorological stations to analyze the spatiotemporal variations of AI and its influencing factors. It was found that the AI decreased significantly and the dry and wet areas increased and decreased, respectively, on the east and west sides of 100° E, and the duration of sunshine and Pre were the main dominant factors in the declining AI trend [33]. Unlike in the study of Zhao et al. [60], the AI calculated by the ratio of Pre to ET_0 exhibited a downward trend in the Loess Plateau and the boundary of dry land region was expanded there [64], and Pre was the main cause of AI variations. Although southwest China became wetter during the past 54 years, Li et al. [37] demonstrated that the region was getting drier over the past 20 years, and decreasing Pre and increasing maximum air temperature were the main factors of the upward AI trend.

In this study, during the growing season and annual time scale, the AI (Pre/ET_0) in the entire, upper, and middle HRB presented an upward trend, which manifested in the HRB becoming wetter in the past 54 years in these regions. However, the Yi-Shu-Si basin and lower HRB became drier with decreasing AI trends. Different from the above studies, this research further analyzed the seasonal variation trends of AI, and the results showed that the AI in the whole HRB and all subregions exhibited a decreasing trend in spring and autumn (becoming drier) and an increasing trend in summer and winter (becoming wetter). From Figure 9 and Supplementary Table S3, we can see that u_2 and R_s were the main dominant factors in annual time scale and growing season, respectively, and these results were echoed in the findings of Wu et al. [65], who reported that wind speed and sunshine hours contributed more to AI trends. In addition, Pre was the main dominant factor in the AI trends in all seasons except for summer, when R_s had a greater effect. Furthermore, we also quantified the effects of Pre and ET_0 on AI trends and found that the contribution of ET_0 was higher than that of Pre in the growing season and annual time scale, while the phenomenon was reversed in all seasons except for summer. Yin et al. [66] also reported that, due to the greater impact of climate change on increasing atmospheric moisture demand (ET_0), most areas of Eastern China are likely to face an increased risk of drought despite the positive Pre anomalies. This further stresses the importance of evapotranspiration demand in drought variation research in the context of future climate warming. All of the above findings are in good agreement with those in a recent study of Liu et al. [45].

In general, extreme droughts related to ENSO (El Niño-Southern Oscillation) events that have greatly affected the vegetation and ecosystem in China [67]. Long-term high-resolution grids of climatic dataset (1950–2000) in southwest China reveals that annual precipitation during May and October is decreasing with fluctuation, whereas at the same time, the mean annual air temperature is increasing in southwest China [68]. Tan et al. [69] stated that the trend of drying is in phase with the enhancing El Niño activities and warming which increased drought episodes in southwest China in the last several decades and consequently the potential water resource crisis and ecological risk may occur under the background of well-known global warming scenarios. In the interannual timescale, the warm-dry climatic trend is associated to the tropical Pacific warming that enhanced ENSO and the weakening of the summer monsoon related to an overall ITCZ (Intertropical Convergence Zone) shift in the Indo-Pacific region [67–69]. Gu et al. [68] reported that aridity index is strongly associated with ENSO events in southwest China. Our study can be inferred that aridity index may be linked to ENSO activities in Eastern China which deserves further investigation.

There have been significant abrupt variations in AI values in the HRB, Eastern China. The basic features of atmospheric circulation (e.g., sea level pressure, wind, temperature) over the study region were analyzed, which was impacted on the AI. The difference between high and low AI years was taken into consideration in this study, and the large-scale atmospheric oscillation indices have substantially impacted on the extreme climatic events. Thus, to compute the variation in atmospheric oscillation, we quantified the average circulation composites and then explored the role of circulation variations

on the trends in extreme aridity. First, we identified the high AI years (1984, 1991, 1998, and 2003) and low AI years (1988, 2001, and 2013) during the study period in the HRB. Next, the change in circulation patterns was computed by the differences between high AI and low AI years based on the ERA5 reanalysis dataset.

Figure 12a exhibits the difference in sea level pressure between high AI and low AI years. The sea level pressure declined overall up to 50 hPa, and thus pressure will decrease the weakening impact of atmosphere on solar radiation, and this will elevate the climate warming. In Figure 12b, summer temperature showed a rising trend overall, hence, warm moist air brings from the ocean during summer may be resultant in higher summer temperature and triggers a warming, which was distributed in the Eastern China. In addition, the northeasterly wind in Eastern China was strengthened, which lessen the extent of the winter monsoon in the north and declined the incursions of colder air, that led to warming in the HRB in winter season (Figure 12c). As seen from Figure 12d, the higher changes in the monthly average geopotential height (500 hPa) happened in summer (near 30 gpm) in the HRB, Eastern China, and a Eurasian continent anticyclone centered was formed in upper portion (near 45° N and 95° E) and there is no visible anticyclone centered on the study area. Furthermore, a cyclone also happened in the western Pacific (near 40° N and 130° E), which suggested a weakening eastern Asian summer monsoon during these high and low AI years. Eastern China consists of large areas with elevated geopotential height differences, forming a ridge with relatively higher geopotential heights. The ridge pattern is located under the anticyclone centered on the top of the study area. A large region of sinking air or a deep warm air mass will both lead to form ridge pattern. Since air is often sinking within a ridge pattern, it tends to bring warmer and drier weather which is unfavorable for the formation of rain. The ridge pattern of high pressure was also related to the high temperature in the ocean which triggered in substantial warming along the east coast of China as well as adverse ecological effects. The incident of persistent higher geopotential height anomalies and dry weather will increase due to global climate warming. This is in good agreement with the findings of the earlier studies [70].

Moreover, agricultural crop production is also highly sensitive to variations in climate factors. Research on the spatiotemporal patterns of ET_0 and AI and their contributing factors can provide reference information for irrigation management and solutions to the climate change situation. The HRB is a major grain-producing base in China, where the major crops include winter wheat, paddy rice, and summer maize. These crops have been proven to be easily affected by variable climate, such as significantly increasing T_a, decreasing u_2 and R_s, and slightly decreasing RH [6,8]. Against the background of climate change, more challenges, including extreme flood, drought [42], and water losses [71], are faced by agricultural crop production and water management in the HRB.

In the lower HRB, ET_0 showed a slightly upward trend and ultimately led to a decrease in AI. Generally speaking, water requirements of various crops and vegetation will be enhanced, especially in the lower HRB, on account of decreasing Pre and increasing ET_0. Similar phenomena also occur in spring and autumn. Ultimately, decreased AI could lead to decreased water availability, crop yields, and agricultural productivity. More specifically, as shown in Table 1 and Figures 4 and 5, the increasing trend of Pre and significant decreasing trend of ET_0 in summer in combination with abundant rainfall will promote more water storage and vegetation growth. Although more irrigation water is required for crop production, excessive Pre concentrated in the monsoon season (June–September) could have an extremely uneven spatial distribution and cause oversaturated soil and even increase the frequency of flood disasters and water logging [72]. In addition, the increasing AI trend with increasing Pre and slightly decreasing ET_0 in winter could also maintain the soil moisture condition, which would benefit the seeding, tilling, overwintering, and regreening periods of winter wheat. In contrast, the AI in spring and autumn showed a downward trend, especially in the upper and lower HRB, which showed a faster decreasing AI trend than other areas. All of these would also adversely affect the growth of winter wheat and summer maize. Gao et al. [73] reported that the increasing trend of drought and the effect on yield were the greatest in the regreening and heading periods of winter wheat in the HRB. Furthermore, except for jointing and tasseling stages, summer maize showed water deficit in

other growth stages [74]. Moreover, the increasing AI trend in the upper and lower HRB in spring deserves further attention, especially in the lower HRB, which showed a significant increasing ET_0 trend (Table 1). Thus, analyzing the spatiotemporal evolution of ET_0 and AI trends and determining the causes in the HRB will be beneficial for farmers and policy makers to implement reasonable irrigation management and focus on the sustainable utilization of irrigation water resources considering climate change. Furthermore, the anthropogenic impacts of land use change, rapid urbanization linked to atmospheric teleconnection should be considered in future research.

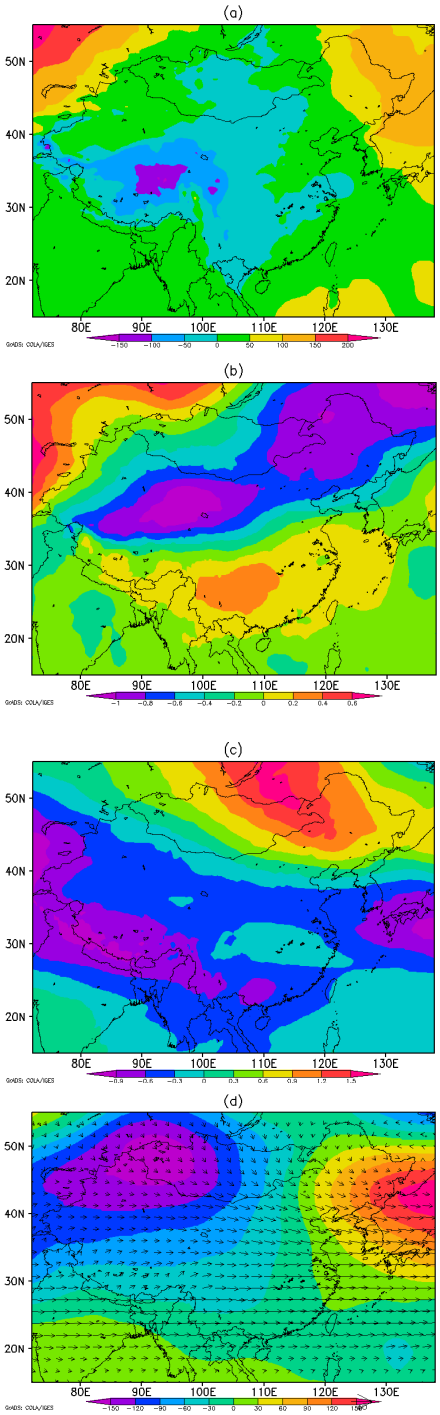

Figure 12. Spatial differences in sea level pressure (**a**), air temperature in summer (**b**), air temperature in winter (**c**), geopotential height and wind speed in summer (**d**) at 500 hPa between high AI and low AI years.

6. Conclusions

In the present study, spatiotemporal variations of Pre, ET_0, and AI were investigated. The dominant factors influencing ET_0 and AI trends were also explored in this study. The study indicated that the leading factors and the order of influencing factors of ET_0 trends calculated by the detrending method are highly consistent with those calculated by the differential equation method. Pre, ET_0 and AI were much larger in summer than in other seasons. AI had a nonsignificant increasing trend in annual time scale, while Pre and ET_0 exhibited decreasing trends. However, AI showed a downward trend in spring and autumn (becoming drier) and an upward trend during summer and winter due to increased Pre (becoming wetter). Overall, lower AI values were identified in the north and higher in the south. Lower ET_0 was identified in the south and higher in the north annually and in growing season and spring, while ET_0 decreased from west to east in summer and winter. The spatial distribution of Pre was similar to that of AI. The original ET_0 indicated a significant decreasing trend, thus the detrended ET_0 was larger than the original one; the detrended AI and Pre were not distinguished from the original, as they did not change obviously. For ET_0 trends, u_2 was the dominant factor of ET_0 trends in spring, autumn, winter and annual time scale, while in other seasons (growing season and summer), R_s played a dominant role. For AI trends, AI was mostly contributed by Pre in spring, autumn and winter, the R_s contributed the most to AI trends in growing season and summer, then in annual time scale, u_2 was the dominant factor. In general, the contribution of Pre was much larger than ET_0 in spring, autumn and winter, which only showed a positive contribution in winter. Moreover, AI was mostly contributed by ET_0 in summer. Thus, AI was dominated by ET_0 in annual time scale and growing season, which was the result of the positive and negative contributions of Pre in different seasons offset each other. The outcomes of the study are important for evaluating limited water resources and irrigation management to adapt measures to control aridity in these susceptible regions throughout the HRB. A better understanding of the mechanisms that influence the ET_0 and AI changes will assist to further variations in the dryness climatic characteristics in the HRB.

Supplementary Materials: The following are available online at http://www.mdpi.com/2071-1050/12/5/1743/s1. Figure S1. Annual variation characteristics of aridity index (AI), reference evapotranspiration (ET_0) and precipitation (Pre).; Table S1. Seasonal and annual trend analysis of climatic factors in each region of the HRB during 1961–2014.; Table S2. Contributions of climatic factors to ET_0 trends in each time scale and subregion of the HRB when using the detrending method (R_{ET0}) and the differential equation method (C_{ET0}, $mm{\cdot}a^{-2}$).; Table S3. Contributions of Pre and four main climatic factors to AI trends in each time scale and subregion of the HRB.; Table S4. Contributions of Pre and ET_0 to AI trends in each time scale and subregion of the HRB.

Author Contributions: M.L. and R.C. designed and wrote the paper; A.R.M.T.I. revised the manuscript; Y.J. and S.S. reviewed and provided some comments for this paper. All authors have read and agreed to the published version of the manuscript.

Funding: This research was funded by the National Natural Science Foundation of China, grant number 41905100; Anhui Provincial Natural Science Foundation, grant number 1908085QD171; Anhui Agricultural University Science Foundation for Young Scholars, grant number 2018zd07; Anhui Agricultural University Introduction and Stabilization of Talent Fund, grant number yj2018-57; National Key Research and Development Project, grant number 2018YFD0300905; Postgraduate Research and Practice Innovation Program of Jiangsu Province, grant number KYCX17_0885.

Conflicts of Interest: The authors declare that they have no conflict of interest.

References

1. Piao, S.; Ciais, P.; Huang, Y.; Shen, Z.; Peng, S.; Li, J.; Zhou, L.; Liu, H.; Ma, Y.; Ding, Y.; et al. The impacts of climate change on water resources and agriculture in China. *Nature* **2010**, *467*, 43–51. [CrossRef] [PubMed]
2. IPCC. Climate change: Impacts, adaptation, and vulnerability. In *Summary for Policymakers*; Report of Working Group II of the Intergovernmental Panel on Climate Change; Cambridge University Press: Cambridge, UK, 2007.
3. IPCC. *Climate Change 2013: The Physical Science Basis*; Cambridge University Press: Cambridge, UK, 2013.
4. Huang, J.; Yu, H.; Guan, X.; Wang, G.; Guo, R. Accelerated dryland expansion under climate change. *Nat. Clim. Chang.* **2016**, *6*, 166–171. [CrossRef]

5. Moral, F.J.; Paniagua, L.L.; Rebollo, F.J.; García-Martín, A. Spatial analysis of the annual and seasonal aridity trends in Extremadura, southwestern Spain. *Theor. Appl. Climatol.* **2017**, *130*, 917–932. [CrossRef]
6. Li, M.; Chu, R.; Shen, S.; Islam, A.R.M.T. Dynamic analysis of pan evaporation variations in the Huai River Basin, a climate transition zone in eastern China. *Sci. Total Environ.* **2018**, *625*, 496–509. [CrossRef] [PubMed]
7. Xu, C.; Gong, L.; Jiang, T.; Chen, D.; Singh, V.P. Analysis of spatial distribution and temporal trend of reference evapotranspiration and pan evaporation in Changjiang (Yangtze River) catchment. *J. Hydrol.* **2006**, *327*, 81–93. [CrossRef]
8. Li, M.; Chu, R.; Shen, S.; Islam, A.R.M.T. Quantifying climatic impact on reference evapotranspiration trends in the Huai River Basin of eastern China. *Water* **2018**, *10*, 144. [CrossRef]
9. Dinpashoh, Y.; Jhajharia, D.; Fakheri-Fard, A.; Singh, V.P.; Kahya, E. Trends in reference crop evapotranspiration over Iran. *J. Hydrol.* **2011**, *399*, 422–433. [CrossRef]
10. Huo, Z.; Dai, X.; Feng, S.; Kang, S.; Huang, G. Effect of climate change on reference evapotranspiration and aridity index in arid region of China. *J. Hydrol.* **2013**, *492*, 24–34. [CrossRef]
11. Tang, B.; Tong, L.; Kang, S.; Zhang, L. Impacts of climate variability on reference evapotranspiration over 58 years in the Haihe river basin of north China. *Agric. Water Manag.* **2011**, *98*, 1660–1670. [CrossRef]
12. Zhao, L.; Xia, J.; Sobkowiak, L.; Li, Z. Climatic Characteristics of Reference Evapotranspiration in the Hai River Basin and Their Attribution. *Water* **2014**, *6*, 1482–1499. [CrossRef]
13. Hobbins, M.T.; Dai, A.; Roderick, M.L.; Farquhar, G.D. Revisiting the parameterization of potential evaporation as a driver of long-term water balance trends. *Geophys. Res. Lett.* **2008**, *35*, 1–6. [CrossRef]
14. Donohue, R.J.; McVicar, T.R.; Roderick, M.L. Assessing the ability of potential evaporation formulations to capture the dynamics in evaporative demand within a changing climate. *J. Hydrol.* **2010**, *386*, 186–197. [CrossRef]
15. Matsoukas, C.; Benas, N.; Hatzianastassiou, N.; Pavlakis, K.G.; Kanakidou, M.; Vardavas, I. Potential evaporation trends over land between 1983–2008: Driven by radiative fluxes or vapour-pressure deficit? *Atmos. Chem. Phys.* **2011**, *11*, 7601–7616. [CrossRef]
16. Liu, Q.; McVicar, T.R. Assessing climate change induced modification of Penman potential evaporation and runoff sensitivity in a large water-limited basin. *J. Hydrol.* **2012**, *464–465*, 352–362. [CrossRef]
17. Roderick, M.L.; Farquhar, G.D. The cause of decreased pan evaporation over the past 50 years. *Science* **2002**, *298*, 1410–1411.
18. Roderick, M.L.; Farquhar, G.D. Changes in Australian pan evaporation from 1970 to 2002. *Int. J. Climatol.* **2004**, *24*, 1077–1090. [CrossRef]
19. Cong, Z.T.; Yang, D.W.; Ni, G.H. Does evaporation paradox exist in China? *Hydrol. Earth Syst. Sci.* **2009**, *13*, 357–366. [CrossRef]
20. Tabari, H.; Marofi, S. Changes of pan evaporation in the west of Iran. *Water Resour. Manag.* **2011**, *25*, 97–111. [CrossRef]
21. Limjirakan, S.; Limsakul, A. Trends in Thailand pan evaporation from 1970 to 2007. *Atmos. Res.* **2012**, *108*, 122–127. [CrossRef]
22. Vicente-Serrano, S.M.; Bidegain, M.; Tomas-Burguera, M.; Dominguez-Castro, F.; Kenawy, A.E.; McVicar, T.R.; Azorin-Molina, C.; López-Moreno, J.I.; Nieto, R.; Gimeno, L.; et al. A comparison of temporal variability of observed and model-based pan evaporation over Uruguay (1973–2014). *Int. J. Climatol.* **2018**, *38*, 337–350. [CrossRef]
23. Peterson, T.C.; Golubev, V.S.; Groisman, P.Y. Evaporation losing its strength. *Nature* **1995**, *377*, 687–688. [CrossRef]
24. Brutsaert, W.; Parlange, M.B. Hydrologic cycle explains the evaporation paradox. *Nature* **1998**, *396*, 30. [CrossRef]
25. Du, H.; Xia, J.; Zeng, S. Regional frequency analysis of extreme precipitation and its spatio-temporal characteristics in the Huai River Basin, China. *Nat. Hazards* **2013**, *70*, 195–215. [CrossRef]
26. Xia, J.; She, D.; Zhang, Y.; Du, H. Spatio-temporal trend and statistical distribution of extreme precipitation events in Huaihe River Basin during 1960–2009. *J. Geogr. Sci.* **2012**, *22*, 195–208. [CrossRef]
27. Shi, P.; Qiao, X.; Chen, X.; Zhou, M.; Qu, S.; Ma, X.; Zhang, Z. Spatial distribution and temporal trends in daily and monthly precipitation concentration indices in the upper reaches of the Huai River, China. *Stoch. Environ. Res. Risk Assess.* **2014**, *28*, 201–212. [CrossRef]

28. Li, Z.; He, Y.; Wang, P.; Theakstone, W.H.; An, W.; Wang, X.; Lu, A.; Zhang, W.; Cao, W. Changes of daily climate extremes in southwestern China during 1961–2008. *Glob. Planet. Chang.* **2012**, *80–81*, 255–272.
29. Croitoru, A.E.; Piticar, A.; Imbroane, A.M.; Burada, D.C. Spatiotemporal distribution of aridity indices based on temperature and precipitation in the extra-Carpathian regions of Romania. *Theor. Appl. Climatol.* **2013**, *112*, 597–607. [CrossRef]
30. Ashraf, B.; Yazdani, R.; Mousavi-Baygi, M.; Bannayan, M. Investigation of temporal and spatial climate variability and aridity of Iran. *Theor. Appl. Climatol.* **2014**, *118*, 35–46. [CrossRef]
31. Muhire, I.; Ahmed, F. Spatiotemporal trends in mean temperatures and aridity index over Rwanda. *Theor. Appl. Climatol.* **2016**, *123*, 399–414. [CrossRef]
32. Zhang, K.; Pan, S.; Zhang, W.; Xu, Y.; Cao, L.; Hao, Y.; Wang, Y. Influence of climate change on reference evapotranspiration and aridity index and their temporal-spatial variations in the Yellow River Basin, China, from 1961 to 2012. *Quat. Int.* **2015**, *380–381*, 75–82. [CrossRef]
33. Chu, R.; Li, M.; Islam, A.R.M.T.; Fei, D.; Shen, S. Attribution analysis of actual and potential evapotranspiration changes based on the complementary relationship theory in the Huai River basin of eastern China. *Int. J. Climatol.* **2019**, *39*, 4072–4090. [CrossRef]
34. Li, M.; Chu, R.; Islam, A.R.M.T.; Shen, S. Reference Evapotranspiration Variation Analysis and Its Approaches Evaluation of 13 Empirical Models in Sub-Humid and Humid Regions: A Case Study of the Huai River Basin, Eastern China. *Water* **2018**, *10*, 493. [CrossRef]
35. Tabari, H.; Talaee, P.H.; Nadoushani, S.S.M.; Willems, P.; Marchetto, A. A survey of temperature and precipitation based aridity indices in Iran. *Quat. Int.* **2014**, *345*, 158–166. [CrossRef]
36. Tabari, H.; Aghajanloo, M.-B. Temporal pattern of aridity index in Iran with considering precipitation and evapotranspiration trends. *Int. J. Climatol.* **2013**, *33*, 396–409. [CrossRef]
37. Li, Y.; Feng, A.; Liu, W.; Ma, X.; Dong, G. Variation of aridity Index and the role of climate variables in the southwest China. *Water* **2017**, *9*, 743. [CrossRef]
38. Liu, X.; Zhang, D.; Luo, Y.; Liu, C. Spatial and temporal changes in aridity index in northwest China: 1960 to 2010. *Theor. Appl. Climatol.* **2013**, *112*, 307–316. [CrossRef]
39. Ahani, H.; Kherad, M.; Kousari, M.R.; Roosmalen, L.v.; Aryanfar, R.; Hosseini, S.M. Non-parametric trend analysis of the aridity index for three large arid and semi-arid basins in Iran. *Theor. Appl. Climatol.* **2013**, *112*, 553–564. [CrossRef]
40. Wu, Y.; Yao, H.; Wang, G.; Shen, G.; Shi, R.; Hou, B. Analysis on characteristics of extreme drought and flood events in Huaihe River Basin. *Hydro-Sci. Eng.* **2011**, *4*, 149–153.
41. Chu, R.; Li, M.; Shen, S.; Islam, A.R.M.T.; Cao, W.; Tao, S.; Gao, P. Changes in reference evapotranspiration and its contributing factors in Jiangsu, a major economic and agricultural province of eastern China. *Water* **2017**, *9*, 486. [CrossRef]
42. He, Y.; Ye, J.; Yang, X. Analysis of the spatio-temporal patterns of dry and wet conditions in the Huai River Basin using the standardized precipitation index. *Atmos. Res.* **2015**, *166*, 120–128. [CrossRef]
43. Allen, R.G.; Pereira, L.S.; Raes, D.; Smith, M. *Crop Evapotranspiration-Guidelines for Computing Crop Water Requirements-FAO Irrigation and Drainage Paper 56*; FAO: Rome, Italy, 1998.
44. Nouri, M.; Bannayan, M. Spatiotemporal changes in aridity index and reference evapotranspiration over semi-arid and humid regions of Iran: Trend, cause, and sensitivity analyses. *Theor. Appl. Climatol.* **2019**, *136*, 1073–1084. [CrossRef]
45. Liu, L.; Wang, Y.; You, N.; Liang, Z.; Qin, D.; Li, S. Changes in aridity and its driving factors in China during 1961–2016. *Int. J. Climatol.* **2019**, *39*, 50–60. [CrossRef]
46. Theil, H. *A Rank Invariant Method of Linear and Polynomial Regression Analysis*; Nederlandse Akademie Van Wetenschappen: Amsterdam, The Netherlands, 1950.
47. Sen, P.K. Estimates of the Regression Coefficient Based on Kendall's Tau. *J. Am. Stat. Assoc.* **1968**, *63*, 1379–1389. [CrossRef]
48. Mann, H.B. Nonparametric test against trend. *Econometrica* **1945**, *13*, 245–259. [CrossRef]
49. Shi, Z.; Xu, L.; Yang, X.; Guo, H.; Dong, L.; Song, A.; Zhang, X.; Shan, N. Trends in reference evapotranspiration and its attribution over the past 50 years in the Loess Plateau, China: Implications for ecological projects and agricultural production. *Stoch. Environ. Res. Risk Assess.* **2017**, *31*, 257–273. [CrossRef]
50. Lin, C.; Yang, K.; Qin, J. Observed surface and upper-air wind speed changes over China since 1960. *J. Clim.* **2012**, *26*, 2891–2903. [CrossRef]

51. Kwon, M.; Jhun, J.-G.; Ha, K.-J. Decadal change in east Asian summer monsoon circulation in the mid-1990s. *Geophys. Res. Lett.* **2007**, *34*, L21706. [CrossRef]
52. Huang, J.; Minnis, P.; Lin, B.; Wang, T.; Yi, Y.; Hu, Y.; Sun-Mack, S.; Ayers, K. Possible influences of Asian dust aerosols on cloud properties and radiative forcing observed from MODIS and CERES. *Geophys. Res. Lett.* **2006**, *33*, L06824. [CrossRef]
53. Guo, H.; Xu, M.; Hu, Q. Changes in near-surface wind speed in China: 1969–2005. *Int. J. Climatol.* **2011**, *31*, 349–358. [CrossRef]
54. Tao, Y.; Huang, Y.; Yang, Y.; Wang, K.; Cheng, X.; Wang, M.; Wu, R. Impact of Urbanization on wind speed in Anhui Province. *Clim. Chang. Res.* **2016**, *12*, 519–526.
55. Che, H.Z.; Shi, G.Y.; Zhang, X.Y.; Arimoto, R.; Zhao, J.Q.; Xu, L.; Wang, B.; Chen, Z.H. Analysis of 40 years of solar radiation data from China, 1961–2000. *Geophys. Res. Lett.* **2005**, *32*, L06803. [CrossRef]
56. Qian, Y.; Wang, W.; Leung, L.R.; Kaiser, D.P. Variability of solar radiation under cloud-free skies in China: The role of aerosols. *Geophys. Res. Lett.* **2007**, *34*, L12804. [CrossRef]
57. Stjern, C.W.; Kristjánsson, J.E.; Hansen, A.W. Global dimming and global brightening-an analysis of surface radiation and cloud cover data in northern Europe. *Int. J. Climatol.* **2009**, *29*, 643–653. [CrossRef]
58. Fei, Y.; Xia, X. Decadal variations of aerosol-cloud-radiation in eastern China and their relationships during 1980–2009. *Meteorol. Environ. Sci.* **2016**, *39*, 1–9.
59. Lin, C.; Yang, K.; Huang, J.; Tang, W.; Qin, J.; Niu, X.; Chen, Y.; Chen, D.; Lu, N.; Fu, R. Impacts of wind stilling on solar radiation variability in China. *Sci. Rep.* **2015**, *5*, 15135. [CrossRef]
60. Zhao, Y.; Zou, X.; Zhang, J.; Cao, L.; Xu, X.; Zhang, K.; Chen, Y. Spatio-temporal variation of reference evapotranspiration and aridity index in the Loess Plateau Region of China, during 1961–2012. *Quat. Int.* **2014**, *349*, 196–206. [CrossRef]
61. Wang, L.; Cao, L.; Deng, X.; Jia, P.; Zhang, W.; Xu, X.; Zhang, K.; Zhao, Y.; Yan, B.; Hu, W.; et al. Changes in aridity index and reference evapotranspiration over the central and eastern Tibetan Plateau in China during 1960–2012. *Quat. Int.* **2014**, *349*, 280–286. [CrossRef]
62. Zhao, Y.; Zou, X.; Cao, L.; Yao, Y.; Fu, G. Spatiotemporal variations of potential evapotranspiration and aridity index in relation to influencing factors over Southwest China during 1960–2013. *Theor. Appl. Climatol.* **2017**, *133*, 711–726. [CrossRef]
63. Zhang, K.; Qian, X.; Liu, P.; Xu, Y.; Cao, L.; Hao, Y.; Dai, S. Variation characteristics and influences of climate factors on aridity index and its association with AO and ENSO in northern China from 1961 to 2012. *Theor. Appl. Climatol.* **2017**, *130*, 523–533. [CrossRef]
64. Wen, M.; Cheng, D.; Song, J.; Zhang, G.; Lai, W.; Jiang, W. Impacts of climate change on aridity index and its spatiotemporal variation in the Loess Plateau of China, from 1961 to 2014. Environ. *Earth Sci.* **2018**, *77*, 137. [CrossRef]
65. Wu, Y.; Zhang, G.; Shen, H.; Xu, Y.J.; Bake, B. Attribute analysis of aridity variability in north Xinjiang, China. *Adv. Meteorol.* **2016**, *2016*, 9610960. [CrossRef]
66. Yin, Y.; Ma, D.; Wu, S.; Pan, T. Projections of aridity and its regional variability over China in the mid-21st century. *Int. J. Climatol.* **2015**, *35*, 4387–4398. [CrossRef]
67. Li, J.; Xie, S.-P.; Cook, E.R.; Huang, G.; Arrigo, R.D.; Liu, F.; Ma, J.; Zheng, X.-T. Interdecadal modulation of El Niño amplitude during the past millennium. *Nat. Clim. Chang.* **2011**, *1*, 114–118. [CrossRef]
68. Gu, Y.; Liu, H.; Traoré, D.D.; Huang, C. ENSO-related droughts and ISM variations during the last millennium in tropical southwest China. *Clim. Dyn.* **2020**, *54*, 649–659. [CrossRef]
69. Tan, L.; Cai, Y.; An, Z.; Cheng, H.; Shen, C.-C.; Gao, Y.; Edwards, R.L. Decreasing monsoon precipitation in southwest China during the last 240 years associated with the warming of tropical ocean. *Clim. Dyn.* **2017**, *48*, 1769–1778. [CrossRef]
70. Tong, S.; Li, X.; Zhang, J.; Bao, Y.; Bao, Y.; Na, L.; Si, A. Spatial and temporal variability in extreme temperature and precipitation events in Inner Mongolia (China) during 1960–2017. *Sci. Total Environ.* **2019**, *649*, 75–89. [CrossRef]
71. Zhang, Y.; Xia, J.; Liang, T.; Shao, Q. Impact of Water Projects on River Flow Regimes and Water Quality in Huai River Basin. *Water Resour. Manag.* **2010**, *24*, 889–908. [CrossRef]
72. Gao, C.; Zhang, Z.; Zhai, J.; Liu, Q.; Yao, M. Research on meteorological thresholds of drought and flood disaster: A case study in the Huai River Basin, China. *Stoch. Environ. Res. Risk Assess.* **2015**, *29*, 157–167. [CrossRef]

73. Gao, C.; Yin, Z.; Xu, Y. Space-time characteristics of drought and flood in main growing periods of winter wheat in Huaihe River Basin and its impact on yield. *Trans. CSAE* **2017**, *33*, 103–111.
74. Gao, C.; Li, X.; Sun, Y.; Zhou, T.; Luo, G.; Chen, C. Spatiotemporal characteristics of water requirement and agricultural drought during summer maize season in Huaihe River Basin. *Acta Agron. Sin.* **2019**, *45*, 297–309. [CrossRef]